J. Fluid Mech. (2001), *vol.* 444, *pp.* 49–78. Printed in the United Kingdom

The thermal signature of a vortex pair impacting a free surface

By GEOFFREY B. SMITH[1], R. J. VOLINO[2],
R. A. HANDLER[1] AND R. I. LEIGHTON[1]

[1]Naval Research Laboratory, Washington, DC 20375, USA
[2]United States Naval Academy, Annapolis, MD 21402, USA

(Received 17 May 1999 and in revised form 30 March 2001)

The action of a rising vortex pair on the thermal boundary layer at an air–water interface is studied both experimentally and numerically. The objective is to relate variations in the surface temperature field to the hydrodynamics of the vortex pair below. The existence of a thermal boundary layer on the water side of an air–water interface is well known; it is this boundary layer which is disrupted by the action of the vortex system. Experimentally, the vortices were generated via the motion of a pair of submerged flaps. The flow was quantified through simultaneous measurement of both the subsurface velocity field, via digital particle image velocimetry (DPIV), and the surface temperature field, via an infrared (IR) sensitive imager. The results of the physical experiments show a clearly defined disruption of the ambient thermal boundary layer which is well correlated with the vorticity field below. Numerical experiments were carried out in a parameter space similar to that of the physical experiments. Included in the numerical experiments was a simple surfactant model which enabled the exploration of the complex role surface elasticity played in the vortex–free surface interaction. The results of this combined experimental and numerical investigation suggest that surface straining rate is an important parameter in correlating the subsurface flow with the surface temperature field. A model based on surface straining rate is presented to explain the interaction.

1. Introduction

The prediction and measurement of the energy and mass fluxes across the air–water interface over the open ocean are of great importance in a large number of applications. A few examples include the development of coupled ocean–atmospheric models, the monitoring of greenhouse gasses, and the accurate determination of sea surface and bulk temperatures via remote sensors. Progress in any of these areas will depend in large part on an improved understanding of the thin thermal, momentum, and mass boundary layers which exist at the air–water interface.

The following work focuses primarily on the aqueous thermal boundary layer and its response to hydrodynamic forcing. This boundary layer commonly develops as the result of evaporation from the water into the atmosphere. During this process the fluid at the interface is cooled, reducing its temperature below that of the bulk. Because of its reduced temperature this thin layer is commonly referred to as the *cool skin*. The presence and behaviour of the cool skin has been documented by many authors, including Woodcock (1941), Saunders (1969), Liu & Businger (1975), Katsaros *et al.* (1977), Paulson & Simpson (1981), Wick *et al.* (1996), and Donlon & Robinson (1997).

Early work by Saunders (1969) reports that the magnitude of the mean temperature difference between the bulk fluid and the water surface can approach 0.3 K, with fluctuations about the mean of over 0.5 K. Note that fluctuations of this magnitude are large enough to prevent even the direction of the heat flux through the interface from being correctly determined. Saunders (1969), using dimensional analysis, argued that the temperature difference across the interface should be proportional to the heat flux and inversely proportional to the square root of the viscous stress. An arbitrary constant was also necessary, and was estimated to be between 5 and 10. However, very little data were available at that time with which to validate the model, and much of the work which followed focused on better model calibration.

While Saunders' model, and its subsequent derivatives, were based primarily on dimensional arguments, Liu & Businger (1975) used a surface renewal approach, based on the work of Howard (1966), to develop a model for the mean water temperature profile near the interface. In this approach the thermal boundary layer is assumed to undergo a cycle of growth, instability, collapse, and regrowth. These efforts, and others, are thoroughly reviewed in Wick *et al.* (1996). However, a recent work by Donlon & Robinson (1997) concludes that, in general, the present models do a poor job of parameterizing the sea surface temperature difference, or cool skin.

The hypothesis of the current work is that the lack of success of previous models is due to an inadequate consideration of the underlying hydrodynamics of the flow. It is these hydrodynamics which dictate the behaviour of the thermal boundary layer, and it is through this understanding that better models of the thermal boundary layer response may be developed. This approach was also adopted by Katsaros *et al.* (1977) and Leighton, Smith & Tang (1998).

For the present study a flow field well documented in the open literature was chosen to disturb a thermal boundary layer at an air–water interface. A pair of low Reynolds number line vortices was generated by a flap mechanism and allowed to propagate to the free surface (Willmarth *et al.* 1989; Bernal *et al.* 1989; Sarpkaya & Suthon 1991; Hirsa & Willmarth 1994; Hirsa *et al.* 1997; Tsai & Yue 1995). In this case the free surface is cooled by evaporation, as described in Volino & Smith (1999). In addition, the previous studies have shown that the flow generated by the vortex pair is sufficiently complex to capture most of the fundamental hydrodynamics present in much more complicated turbulent flows.

A complete review of the vortex–interface interaction literature is not appropriate here (for a more complete review see Sarpkaya 1996), but a few significant results should be touched upon. In the case of a clean free surface the vortex pair rises to the surface and separates, with each of the two vortices in the pair moving off in different directions (Tsai & Yue 1995). However, when the interface is not clean, the interaction results in a rebound of the primary vortices after they impinge on the free surface (Hirsa & Willmarth 1994). Additionally, the induced surface velocity creates surfactant gradients, which themselves interact with the subsurface flow (Hirsa *et al.* 1997, Tsai & Yue 1995). However, even with only a small concentration of surfactant present, the behaviour of the vortices near the contaminated surface is very similar to that documented in vortex interactions with solid boundaries (Orlandi 1990; Walker *et al.* 1987; Swearingen, Crouch & Handler 1995).

A unique aspect of the present investigation is the simultaneous determination of the velocity beneath the surface and the surface temperature fields. The velocity fields were measured using digital particle image velocimetry (DPIV). Simultaneously, the temperature field at the free surface was determined using a high-resolution infrared (IR) sensing camera.

The majority of the investigations which document the temperature field at a free surface concentrate on free convection-driven flows. A detailed review of these works was conducted by Goldstein & Volino (1995). However, in the majority of these previous works no quantitative, simultaneous measurements were made of the resulting flow field. One of the few laboratory studies which obtained simultaneous measurements was that of Volino & Smith (1999), where the hydrodynamics and thermal signature of free convection were investigated.

2. Experiments

2.1. *Experimental apparatus and methods*

The experimental apparatus is shown schematically in figure 1. All experiments were conducted in a glass walled tank 40 cm long, 20 cm wide, and 25 cm in height. Tap water filtered with 5 μm filters was the working fluid for these investigations, and was used to fill the tank to a depth of approximately 20 cm. The actual tank depth was set before each run to ensure that the tips of the flaps were initially 4.8 cm beneath the water surface. The tank was uncovered, allowing evaporation from the free surface. As discussed in Volino & Smith (1999), the heat flux from the free surface under these conditions is dominated by evaporation (i.e. mass transfer) from the free surface, as opposed to the temperature difference between the free surface and the ambient air. The total loss of mass from the system due to this process was negligible during any of the experiments. Based on free convection correlations, it is estimated that a 0.1 °C change in water surface temperature will result in a $< 1\%$ change in local heat flux. Hence, the assumption of constant and uniform heat flux during the course of each experiment is valid, despite the observed variation in surface temperature. The ambient dry bulb temperature was 22.5 ± 0.5 °C and the wet bulb temperature was 17 ± 1 °C. For all the experiments the bulk water temperature was 22 ± 1 °C, and the mean undisturbed surface temperature was ~ 0.5 °C cooler. The heat flux through the surface due to evaporative cooling was $60 \pm 6\,\mathrm{W\,m^{-2}}$.

The vortex generator consisted of two rotating flaps which were anchored at the bottom of the tank. The flaps themselves were sheets of 0.32 cm thick Plexiglas and were 20.3 cm long by 10.2 cm in height. The upper edges of the flaps were bevelled with approximately a 30° angle. Each flap was attached to a 1.3 cm diameter Plexiglas rod which was supported at each end by a PVC block. The rods were able to rotate in their PVC supports, thereby rotating the flaps. At the start of each run, the flaps were vertical with a 3.8 cm spacing between them. A computer controlled micro-stepper motor was used to rotate the flaps. As they rotated toward one another a line vortex formed at the lip of each of the flaps, parallel to its edge. The speed and angular displacement of the flaps was varied by changing the speed and travel of the stepper. In this manner the strength of the generated vortices could be adjusted. This apparatus is similar in concept to the system used by Hirsa & Willmarth (1994).

The vortex interactions with the free surface were quantified using both an infrared detector and a digital particle image velocimetry system. The infrared imaging system (Raytheon-Amber AE4256) consisted of the imaging array, a liquid nitrogen dewer with filters, a digital acquisition system, and other ancillary electronics. The array itself was $\sim 9.7\,\mathrm{mm}^2$ in area, and consisted of 256×254 pixels. A filter window at the front of the array passed radiation in the 3–5 μm band. The optical depth (defined here as the depth below which a negligible amount of radiation can escape from the surface) of water in this band is approximately 25 μm. The noise equivalent temperature

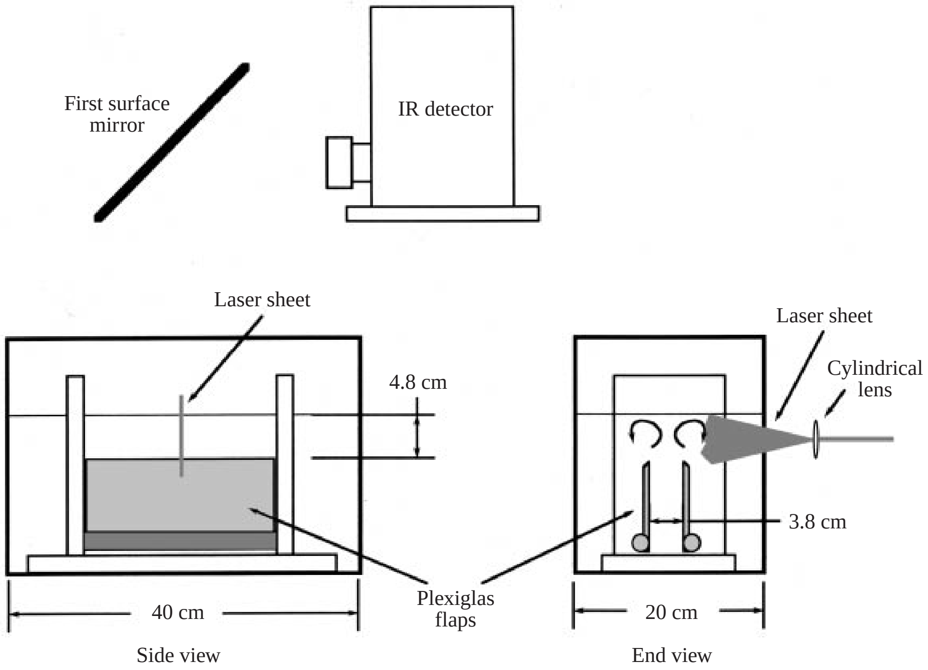

FIGURE 1. Side and end view schematic of the experimental setup. Not shown are the 5 W argon-ion laser, related optics, data acquisition system, and video camera.

change (NEDT) for this system was 0.025 K. This low NEDT was achievable due to the cooling provided to the array by the liquid nitrogen filled dewer. The 12 bit digital output from the camera was captured using a PC based video capture system.

The DPIV system was a typical configuration using a shuttered 5 W argon-ion laser as the light source and a 1134 × 486 pixel Texas Instruments camera operating in dual field mode to capture the images. Custom electronics were developed to synchronize the video signal from the camera with the shuttering of the laser in order to straddle the frame marker, effectively increasing the maximum velocity measurable by the system. This technique is described in greater detail in Smith (1996). Polystyrene encapsulated fluorescein particles (20–40 μm diameter) were used to seed the flow. The images were captured via a PC based video capture system and processed with AEA Visiflow, a commercially available DPIV analysis package.

Two different experimental conditions were considered for these experiments. For both cases the vortices were characterized by their Reynolds number, $Re = \Gamma/\nu$, where Γ is the circulation associated with a single vortex calculated from a DPIV image pair before the vortex was influenced by the interface, and ν is the kinematic viscosity of water. In the low Reynolds number case the flap system produced vortices with $Re \approx 300$ and in the high Reynolds number case $Re \approx 2600$. The settings for the DPIV system vary depending on the flow being interrogated. For the low Reynolds number case the pulse length was set to 5 ms and the time between pulses was set to 33 ms. In the high Reynolds number case the pulse duration was 3 ms and the time between pulses was 4 ms. In both cases these values were chosen to ensure that the maximum velocities were resolved for all the runs.

Velocity vectors were calculated from the acquired images using the AEA Visiflow package. All of the data were evaluated using a square interrogation window with

64 pixels on a side, and a cross-correlation technique was used to calculate the displacements. The data were four times oversampled. Uncertainty in these velocity measurements was typically less than 5%. The details of this technique are outlined in Willart & Gharib (1991), and further details of the actual system used may be found in Volino & Smith (1999). Different fields of view were used for the low and high Reynolds number experiments, yielding spatial resolutions of 3.55 mm and 2.99 mm, respectively.

During all of the experiments the IR camera was looking down at the surface of the tank, as illustrated in figure 1. In this configuration the field of view of the camera was approximately square, 16.6 cm on a side, resulting in a spatial resolution of 0.6 mm. For all of the runs presented here IR temperature data were acquired as 100 image sequences. The framing rate of the camera was held constant at 30 Hz for these experiments, but the time between images in the stored sequences was varied from 0.1 s to 0.067 s, depending on the run. The data acquisition for both the IR and the DPIV was initiated by the same signal which started the flap motion, thereby ensuring that all three processes began at essentially the same instant in time.

2.2. *Experimental results*

2.2.1. *Initial conditions*

Hundreds of infrared images of the water surface acquired during the vortex interaction were closely examined; an example of a typical image is shown in figure 2(*a*) below. This image was taken before the surface had been disturbed by the vortex pair, and therefore is representative of the steady state achieved in the tank before each experimental run. The thermal structure (darker colours represent cooler temperatures and lighter represent warmer) present in this case is due to evaporation-driven convection in the water column, as described by Volino & Smith (1999), Saylor, Smith & Flack (2000), and Katsaros *et al.* (1977). These patterns are remarkably similar to those documented at a solid boundary, as shown by Asaeda & Watanabe (1989). Also visible in figure 2(*a*) is an apparent low-amplitude, large-scale spatial variation in the temperature field; there is a slightly brighter region near the centre of the image, and the edges of the image are slightly darker. This is not an indication of actual temperature variations, but is an artifact of the camera and calibration process. As will be seen below, the presence of this variation does not impede our ability to discern structure in the image and draw conclusions regarding the sub-surface hydrodynamics. Another camera artifact is the small circular dark spot visible in the upper left quadrant of the image. This spot is an image of the cold lens of the array reflected from the water surface.

As is obvious in figure 2(*a*), the surface temperature field is complex, even under simple evaporative cooling. A simple model, based on conduction and surface strain, can be used to help explain the features in the water surface temperature fields. In anticipation of the definitions to be used in the numerical simulations, the x- and y-axes are perpendicular to one another and parallel to the free surface. The y-axis is also parallel to the axis of rotation of the primary vortex. The symbols u and v represent velocities in those directions, respectively.

In the present experiments variations in the x-direction are of primary interest, and the rate of strain, given by

$$S_x = \frac{\partial u}{\partial x}, \tag{2.1}$$

plays a crucial role in understanding the dynamics of the flow. The surface flow is defined to be *divergent* in regions where S_x is positive. A fluid element in the divergent flow will be elongated along the axis of the strain and dilated perpendicular to that axis. The opposite occurs in convergent zones. In a heuristic way we can extend this result to apply to the thickening and thinning of the thermal boundary layer in response to the underlying hydrodynamic straining field. This can be understood by considering a thin layer of fluid near the boundary which is suddenly subject to a divergent straining field, as would be the case between the vortices in these experiments. From a Lagrangian viewpoint, the fluid layer will then be lengthened in x and compressed in z. If diffusion is neglected, the thermal boundary layer will also be deformed in this manner. If the thermal boundary layer is assumed to be initially steady ($\partial \Theta / \partial t = 0$) with an equilibrium thickness given by δ_e, then a linear estimate of the temperature difference across the layer is $\Theta_s - \Theta_b = -(q_s \delta_e)/k$ (Θ_b is the temperature of the bulk, and Θ_s is the water surface temperature) where the surface heat flux, q_s, is held constant and assumed to be positive (surface cooling). The strain field imposed by the vortex pair will compress the layer to a new thickness δ so that the new surface temperature, Θ_s^*, can then be estimated as $\Theta_s^* - \Theta_s = (q_s/k)(\delta_e - \delta)$. Thus, for the case of a vertically compressed thermal layer, $(\delta_e - \delta) > 0$ and the surface temperature increases. For a vertically extended boundary layer, as would be the case for a convergent strain field, the opposite is true and the surface is expected to cool. While this argument is highly idealized, it captures the essential point that since the surface flux is fixed, the surface temperature is expected to correlate well with the thickening and thinning of the thermal boundary layer. A more in-depth discussion of this surface straining model may be found in Leighton *et al.* (2001).

In the context of the present experiments, as the surface is cooled via evaporation a thin layer of cool fluid is created on the water surface. As the Rayleigh number of this unstable configuration increases a critical threshold is eventually crossed, and free convection in the bulk fluid commences. The Rayleigh instability is characterized by narrow descending sheets, or plumes, of cool surface fluid falling into the bulk. To balance this, there are broad regions of warmer ascending fluid approaching the surface from below. In this simplified model the flow near the surface in the vicinity of the narrow descending sheets is parallel to the surface approaching the sheets, and down into the bulk in the sheet itself. The value of S_x for this flow pattern is negative; in other words, there is a convergent flow above the narrow descending plumes. This convergence zone compresses the thermal boundary layer along the x-axis, causing it to expand and thicken in the vertical, or z-direction. The locally thicker thermal boundary layer, along with the constant heat flux assumption, is expected to maintain a region of locally cooler surface temperature. In the broader regions characterized by the ascension of warmer bulk fluid, the converse is true. A weak divergent flow field is generated, resulting in a thinner thermal boundary layer, and correspondingly warmer surface temperatures.

2.2.2. *Infrared results*

Examples from two representative data sets will be presented; the first is obtained from a low Reynolds number vortex ($Re \approx 300$) run, and the second from a high Reynolds number ($Re \approx 2600$) run. Figure 2 contains a set of six images taken from one of the low Reynolds number runs. As previously discussed, these images are plan views of the water surface; there is 7 s between each of the images in the sequence. The vortices were generated beneath the surface with their primary axes parallel to the top and bottom edges of the images.

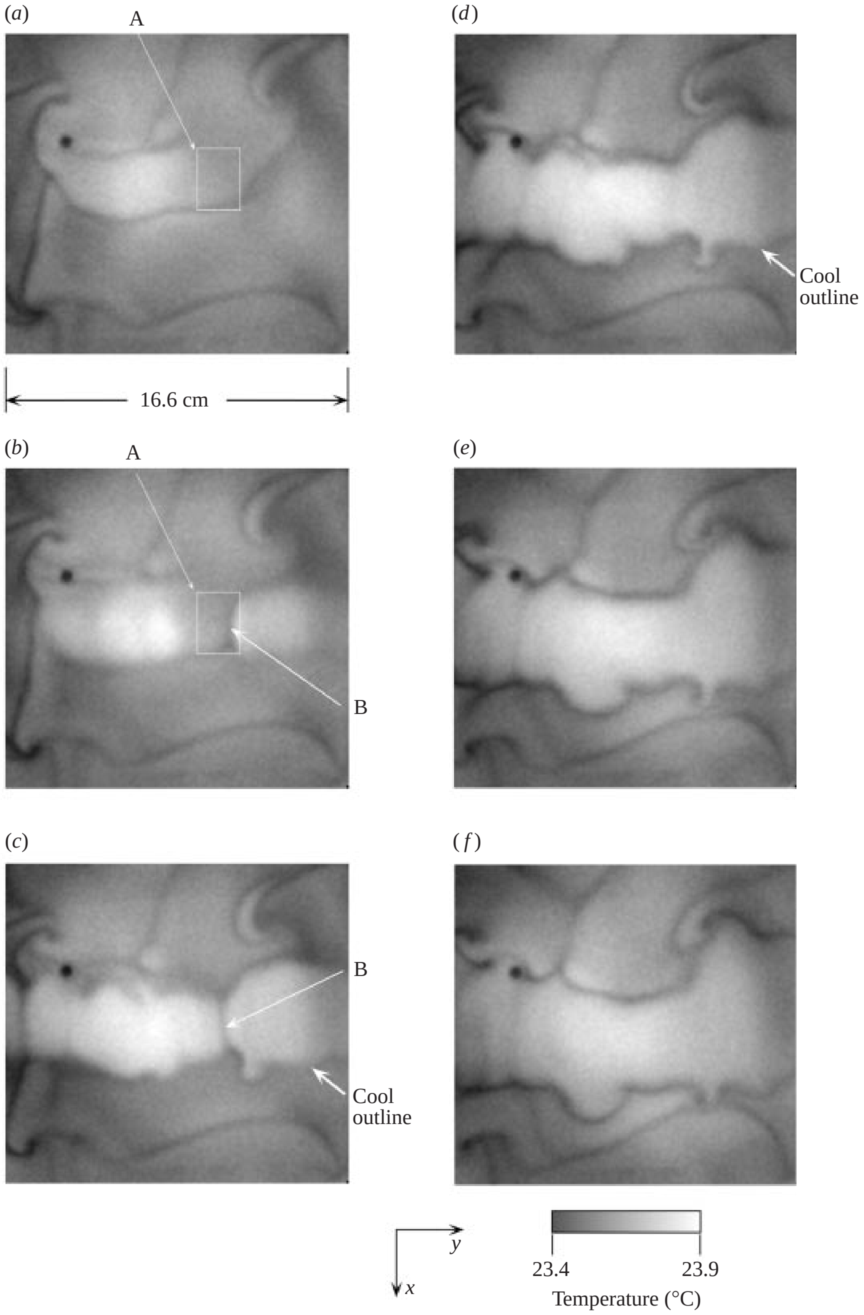

FIGURE 2. Sequence of six IR images taken from a low Reynolds number run, $Re \approx 300$. The vortices were generated beneath the water surface with their primary axes parallel to the top and bottom edges of the images. The camera is looking through a mirror, down on the water surface. The area imaged is approximately 16.6 cm (256 pixels) on a side, and the lighter regions represent warmer temperatures. There is 7 s between each image in this sequence. Time is measured from the initiation of the vortex generator motion, and is given for each of the images in the sequence: (*a*) $t = 7$ s, (*b*) $t = 14$ s, (*c*) $t = 21$ s, (*d*) $t = 28$ s, (*e*) $t = 35$ s, (*f*) $t = 42$ s.

Figure 2(*a*) is a view of the water surface before it has been disturbed by the vortex pair. In figure 2(*b*) the first evidence of the rising vortex pair is visible as regions of warmer surface temperature near the centre of the image. It is in this region in the centre of the image where the flow field associated with the vortex pair will result in a divergent straining field. In the context of the model described above, this hydrodynamic straining thins the thermal boundary layer, and results in the warm region visible in the centre of the image.

It is also apparent that the primary vortices and their interaction with the free surface are not invariant along the y-axis. In particular, the region labelled A in figure 2(a, b) is an area where the surface temperature changes very little over the time interval between the two images. However, an increase in the temperature in the area just to the left of that region is clearly visible. What appears to have occurred is that a descending sheet associated with a cold scar in the surface, marked B, was of sufficient strength to disrupt the upward motion of the vortex pair in that particular area. The peak velocities between the vortices in the pair are on the order of $2\,\mathrm{cm\,s^{-1}}$, while those associated with the descending plumes of the background free convection are expected to be on the order of $0.1\,\mathrm{cm\,s^{-1}}$, as documented in Volino & Smith (1999). Hence, it is not surprising that a particularly strong thermal plume would be energetic enough to locally disrupt the flow generated by the vortex pair. In figure 2(*c*) the primary vortices have affected a larger region of the free surface, creating a wider warm scar in the image. However, the remnant of the downwelling has not yet been totally eliminated by the vortices, and is still visible as B. Figure 2(*d*) shows that the vortex pair has finally eliminated the surface signature of the initial structure, and the temperature in the warm scar has reached a maximum. Figures 2(*e*) and 2(*f*) show the interaction later in time where the peak temperature has decreased slightly, and the spatial scales of the thermal structures have seemingly stabilized.

Clearly visible throughout this sequence is a dark, cool filament which outlines the warm patch generated by the vortices. This filament is indicated by an arrow in figure 2(c, d). While the origin of the outline will be examined in greater detail during the discussion of the numerical results, the generation mechanism can be explained in the context of the surface straining model. In the region between the two vortices (near the centreline of the image), the velocity field associated with the vortices generates a positive rate of surface strain, and the surface temperature is elevated, as predicted by the surface strain model. However, because the surface flow outside the two vortices (near the upper and lower edges of the image) is initially relatively quiescent, there must be a change in the sign of the rate of surface strain, resulting in a region of negative strain rate outlining the warm patch. This must result in an elongated region of convergence which, according to the surface straining model, gives rise to the cool filament outlining the warm patch.

Examination of figure 2(d–f) reveals that during this time interval there is very little change in the spatial structure of the surface temperature field. The only obvious changes are a decrease in the temperature of the warm scar, indicating that the strain field from the vortex pair is no longer intense enough to maintain it. As the vortices weaken, the interface, being cooled by evaporation, returns to a steady state. It is also interesting to note that the dark outlines of the warm scar have remained, and are now apparently being maintained by natural convection.

Figure 3 contains a sequence of images taken from one of the high Reynolds number ($Re \approx 2600$) runs. In this case there is 0.67 s between images in the sequence. Figure 3(*a*) shows the water surface 1.67 s after the start of the run, but before the vortex pair has begun to significantly affect the thermal structure of the surface. In

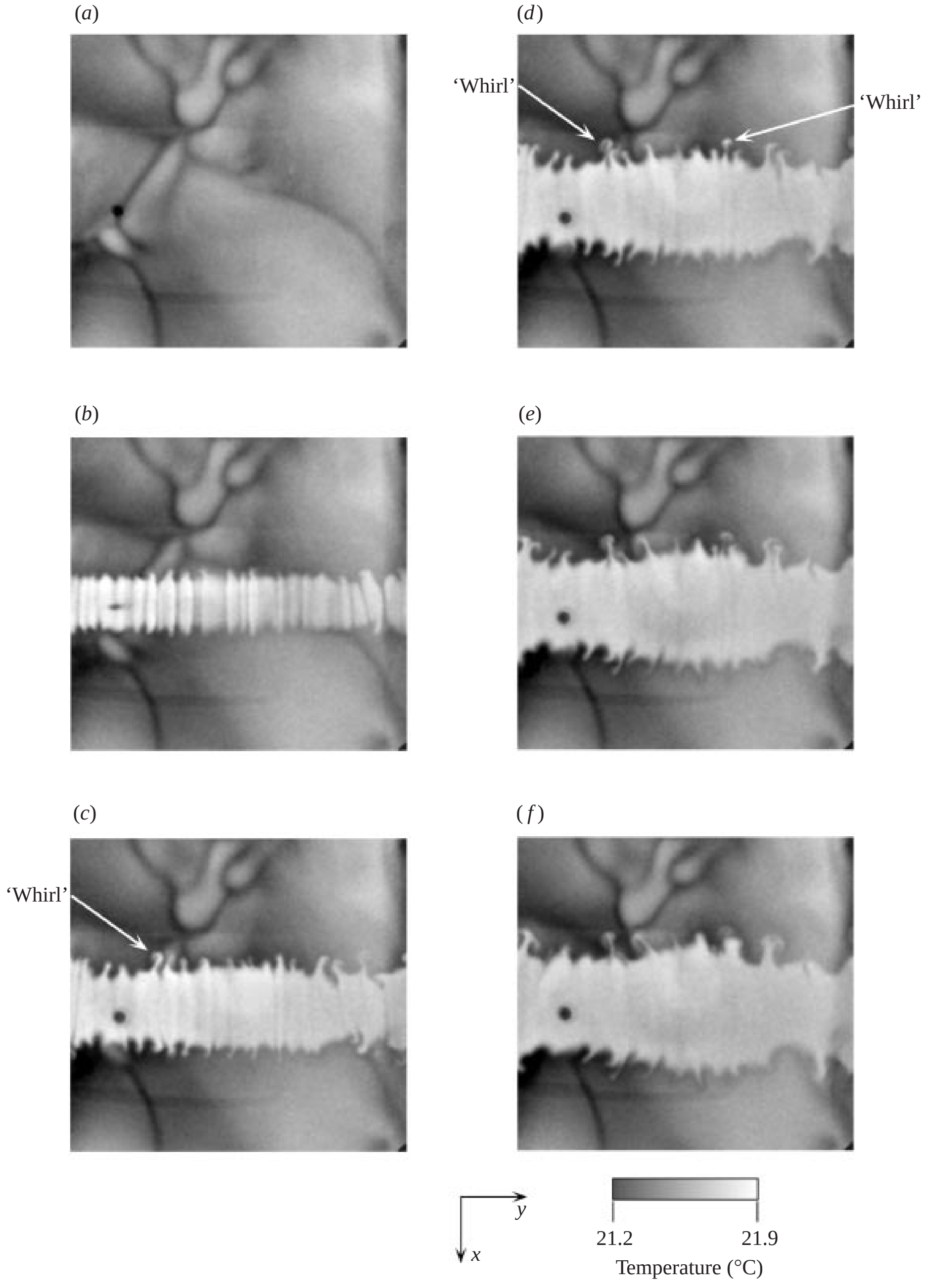

FIGURE 3. Sequence of six IR images taken from a high Reynolds number run, $Re \approx 2600$. The vortices were generated beneath the water surface with their primary axes parallel to the top and bottom edges of the images. Time is measured from the beginning of the vortex generation process, and is: (*a*) $t = 1.67$ s, (*b*) $t = 2.33$ s, (*c*) $t = 3.00$ s, (*d*) $t = 3.67$ s, (*e*) $t = 4.33$ s, (*f*) $t = 5.00$ s.

figure 3(*b*) the vortex pair has caused a clearly visible warm scar on the water surface. There are several comparisons to be made between this frame and the low Reynolds number IR data. First, the primary vortices appear to be much more robust than in the low Reynolds number case. In other words, the two primary vortices are not as distorted by the background natural convection. Secondly, the range of scales visible in the interaction is much larger in this high Reynolds number case.

In figure 3(*c*) the warm scar widens slightly while the small-scale structures continue to evolve. In figure 3(*c, d*) the structures indicated by the arrows are very much like what would be expected from a vortex pair attached to the free surface. Figure 3(*e, f*) again shows slight cooling of the warm patch across the centre of the images, indicating a weakening of the hydrodynamic forcing from below. The spatial structure of the temperature field evolves very little during the time of the last images in this sequence.

There is a striking similarity between the surface temperature data presented here and the shadowgraph results of Sarpkaya & Suthon (1991). Specifically, the scalloped edges of the warm scar are very suggestive of the rippled surface observed by Sarpkaya & Suthon (1991). They report that the source of the signatures, which they term 'whirls' and 'scars', is a short-wavelength instability which is most likely introduced during the creation of the vortex pair. They also report that for Froude numbers ($Fr = \Gamma(4g\pi^2D^3)^{-1/2}$ where g is the acceleration due to gravity and D is the spacing between the vortex cores) less than ~ 0.15 surface deformation and the resulting nonlinear interactions are negligible. The largest Froude number observed in the present experiments was approximately 0.09, indicating that while the surface temperature patterns resemble the shadowgraph results they are most likely not associated with significant surface deformations.

The dark filament (designated as the 'cool outline' in 2*c*) which was so prominent in the low Reynolds number data, is faintly visible in figure 3(*f*). The conditions necessary for its development in the low Reynolds number case also exist in the high Reynolds number runs, so the presence of the outline was not unexpected. A likely explanation for its weaker signature lies in the large disparity of hydrodynamic time scales between the two cases. In the low Reynolds number case the thickening of the thermal boundary layer due to local surface convergence takes place over a relatively long time. The locally thick boundary layer therefore has the opportunity to go unstable and develop into a descending plume. In the high Reynolds number runs the thermal boundary layer also thickens, but the local three-dimensionality and the overall rapidity with which the interaction evolves conspire to disrupt the formation of the cool outline before it has the opportunity to go unstable and evolve into a self-sustaining structure.

2.2.3. *DPIV results*

Two-dimensional velocity fields from (x, z)-planes, perpendicular to the free surface and the primary vortex cores, were obtained simultaneously with the IR sequences presented above. In figure 4 contours of the y-component of vorticity, calculated from DPIV data for a representative run taken from the low Reynolds number case, are shown. All of the DPIV images are of an area roughly 5.75 cm wide by 4 cm deep; in this case there is 1.4 s between each image in the sequence. The line plot above the contour plot is the corresponding surface temperature data extracted from the IR imagery.

The contours plotted in figure 4(*a*) clearly show the primary vortex pair 6.3 s after the beginning of the run. From this point forward the vortex on the left will be referred to as the negative vortex, the vortex on the right as positive. The weaker patches of opposite sign vorticity located just below the primary pair are regions of secondary vorticity generated by the flow around the flaps of the generator. At this time during the interaction the surface temperature is not significantly different from the steady, undisturbed state.

While efforts were made to maintain a clean surface during these experiments, it is acknowledged that there was indeed some surface contamination. This is confirmed by figure 4(*b*), where a layer of secondary vorticity is visible at the surface. The presence of this secondary vorticity is a well-documented phenomenon in instances where the free surface is contaminated (Bernal *et al.* 1989; Sarpkaya & Suthon 1991; Hirsa & Willmarth 1994; Hirsa *et al.* 1997; Tsai & Yue 1995). In the experimental portion of the current work no effort was made to characterize any surfactant present, or to vary its properties. However, the effects of a contaminated surface will be explored in greater detail using the numerical simulations (§ 3.3).

The surface temperature, also shown in figure 4(*b*), has risen ∼ 0.05 °C. The continuation of this trend is seen in figure 4(*c*) where the surface temperature has reached a peak of ∼ 23.7 °C. Note that at this time the primary vortices have propagated almost to the surface, and layers of opposite sign vorticity are apparent above each of the primary vortices. The peak in surface temperature occurs almost directly between the primary vortices, where we expect the strength of the divergence zone should be strongest, and the thermal boundary layer to be thinnest.

Figure 5(*a*–*e*) shows the surface temperature data and surface parallel vorticity for a high Reynolds number case. The data shown in figure 5(*a*) were obtained 2.00 s into the run; there is 0.13 s separating subsequent images. The two primary vortices are clearly visible in the centre of the field of view, propagating upwards, toward the free surface. As in the low Reynolds number case, the development of a layer of vorticity on the underside of the free surface is visible. At this time the free surface temperature has begun to show signs of an increase in the region between the vortices. This is the same phenomenon described in the low Reynolds number example, although the interaction occurs much more rapidly in this case.

In figure 5(*b*, *c*) the primary vortices move closer to the free surface, the layer of secondary vorticity increases in strength, and the surface temperature over the vortex pair continues to increase. In figure 5(*d*) the secondary layer over the negative vortex begins to separate from the free surface. This phenomenon is not as apparent over the positive vortex as its outer edge begins to move out of the field of view. The peak temperature between the vortices continues to increase, and a slight dip begins to develop in the surface temperature at $x \sim 1.7$ cm. This dip strengthens and moves slightly in the negative x-direction in figure 5(*e*), while the peak temperature has risen to ∼ 21.8 °C. The width of the warm thermal scar on the free surface continually increases throughout this interaction while the outer edges of the scar closely track the trajectories of the primary vortices.

Also shown in figure 5(*e*) is the behaviour of the secondary vorticity, which at this time has further detached from the surface and is beginning to be swept around the primary core. While the only vorticity data available are in planes perpendicular to both the free surface and the primary vortex cores, it is speculated that this secondary vorticity is contributing to the small-scale structures seen in the IR imagery. Note that the secondary vorticity is generated with its axis parallel to the primary vortices. Any perturbation of that secondary vorticity will cause it to rotate into an orientation perpendicular to the primary vortex, resulting in regions of opposite sign vorticity imbedded in the outer region of the primary vortex. If, for example, the re-oriented secondary vorticity reconnects with the free surface, the resulting signature in the surface temperature patterns would appear much like the small-scale disturbances (‘whirls’) noted in figure 3.

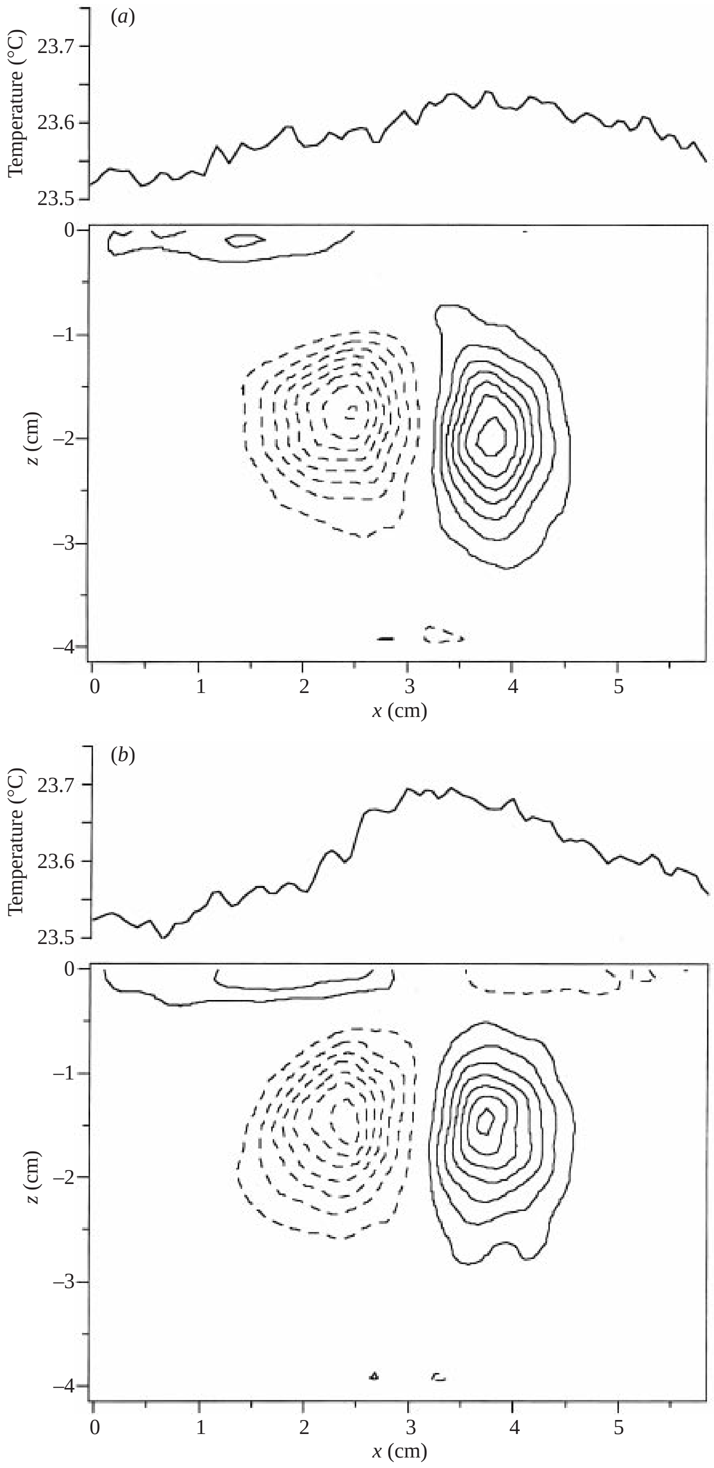

FIGURE 4 (a, b). For caption see facing page.

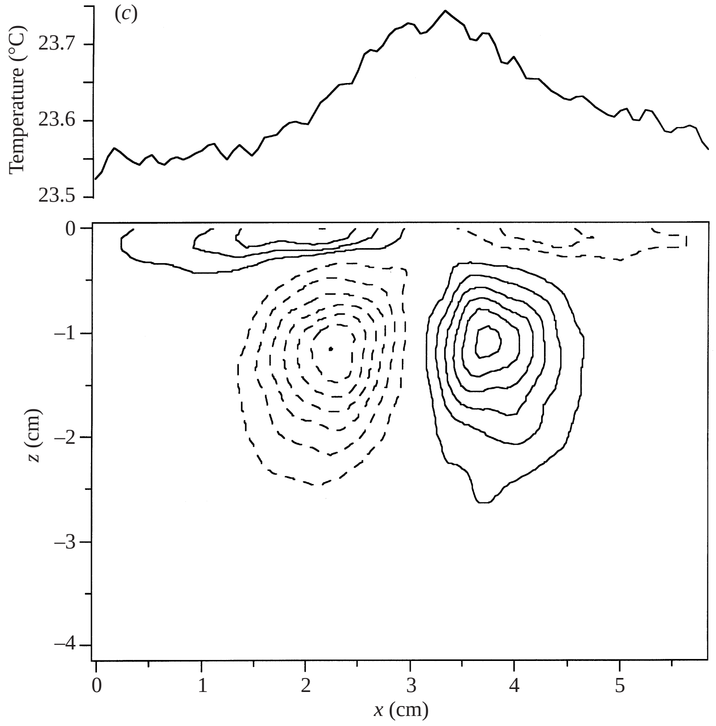

FIGURE 4. Contours represent vorticity (solid lines are positive, and dashed lines are negative) calculated from DPIV velocity data collected concurrently with the IR data presented in figure 2. $Re \approx 300$. The outermost contour of each of the primary vortices are 0.5 and $-0.5\,\mathrm{s}^{-1}$ for the positive and negative vortices respectively, and there is $0.5\,\mathrm{s}^{-1}$ between contours. The line plot above displays a simple second-order binomial fit to the surface temperature data extracted from the IR sequence. (a) $t = 6.3$ s, (*b*) $t = 7.7$ s, (*c*) $t = 9.8$ s.

3. Numerical simulations

Motivated by the experiments described above, a series of numerical simulations was performed to further elucidate the processes involved in vortex pair–free surface interactions, and in particular, to establish in greater detail the relationship between the subsurface hydrodynamics and the surface thermal signature. The experiments described in § 2 have identified several processes which need to be considered in developing an accurate numerical model; these include (i) buoyancy effects, (ii) three-dimensionality, (iii) surface deformation, and (iv) surfactant dynamics. We show below that several of these effects can be reasonably neglected in developing a model which spans the parameter range embodied in the experiments.

3.1. *Problem formulation*

In the experiments, although the thermal boundary layer appears to be statistically steady, significant buoyancy-induced fluctuations in temperature and velocity exist near the free surface. The experimental results at high Reynolds number indicate that the time scales associated with the thermal fluctuations within the thermal boundary layer due to buoyancy-induced instabilities are significantly longer than the time scales associated with the vortex pair itself. Thus, we may reasonably assume that the

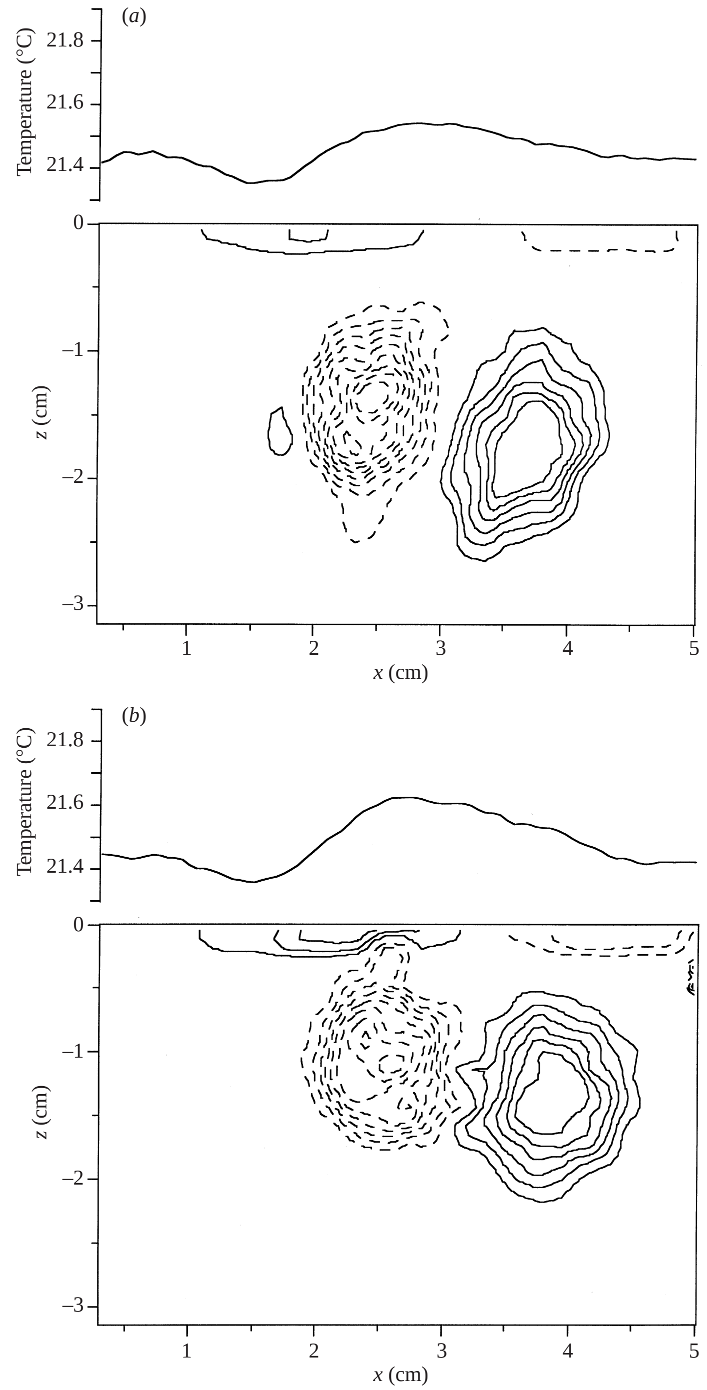

FIGURE 5 (*a*, *b*). For caption see page 64.

dynamics maintaining the thermal boundary layer are decoupled from the vortex pair dynamics. Accordingly, buoyancy forces were not explicitly included in the numerical model.

In the higher Reynolds number experiments ($Re \sim 2600$), instabilities, whose spatial

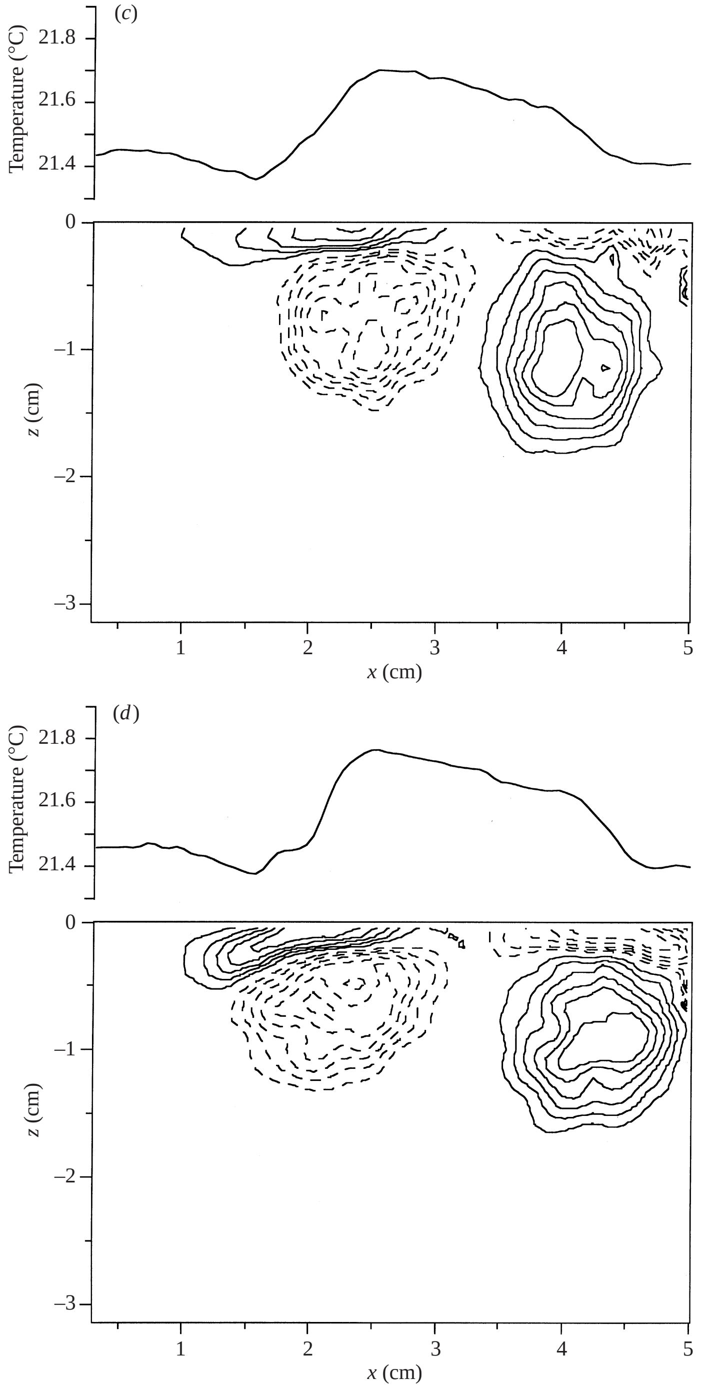

FIGURE 5 (*c*, *d*). For caption see page 64.

scales are small compared with the diameter of the core of the vortex, are apparent in the infrared imagery. These instabilities do not appear to significantly interfere with the development of the thermal scar at the surface, which is caused by the large-scale strain field imposed by the vortex pair. As a result of these observations,

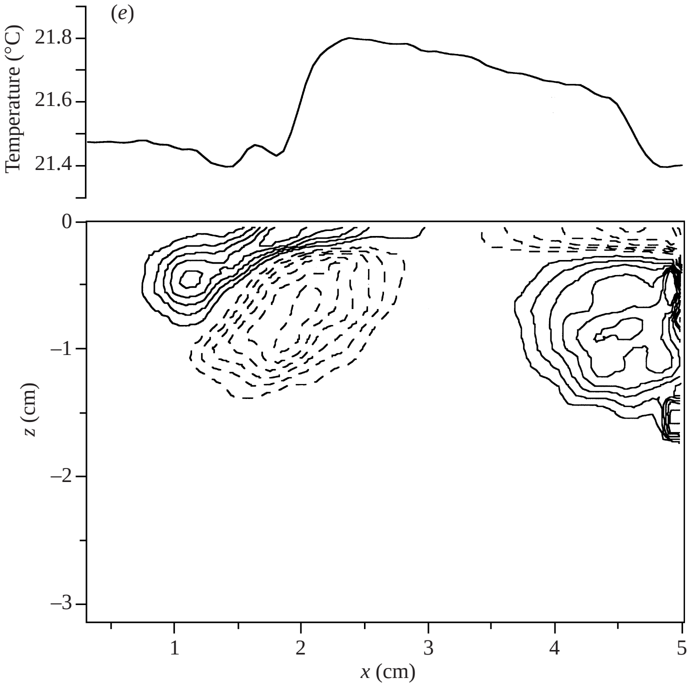

FIGURE 5. As figure 4 but from DPIV velocity data collected concurrently with the IR data presented in figure 3. $Re \approx 2600$. (a) $t = 2.00$ s, (b) $t = 2.13$ s, (c) $t = 2.27$ s, (d) $t = 2.40$ s, (e) $t = 2.53$ s.

we have neglected three-dimensional effects and have used a strictly two-dimensional formulation of the problem.

Effects due to surface deformations are neglected in the flows considered here. The largest Froude number observed in the experiment was approximately 0.09, which is well below the value (~ 0.15) cited by Sarpkaya & Suthon (1991) above which surface deformations become significant. Therefore, the free surface can be modelled as a flat boundary. The effects of surface films were included in the numerical model.

The coordinates (x, y, z) are used, where x and y are the planar or horizontal coordinates (in the plane of the free surface), and z is perpendicular to the boundary. Unit vectors $\hat{\boldsymbol{e}}_x, \hat{\boldsymbol{e}}_y$, and $\hat{\boldsymbol{e}}_z$ are defined in the x-, y-, and z-directions respectively. Since the simulated flow is strictly two-dimensional the velocity is given by $\boldsymbol{V} = U(x,z,t)\hat{\boldsymbol{e}}_x + W(x,z,t)\hat{\boldsymbol{e}}_z$, and $\boldsymbol{\Omega} = \Omega(x,z,t)\hat{\boldsymbol{e}}_y$ is the vorticity. The vortex pair is generated by applying an impulse to the fluid through the use of a vertically oriented body force, $\boldsymbol{F} = F(x,z,t)\hat{\boldsymbol{e}}_z$ (see Swearingen *et al.* 1995 and Chen, Swearingen & Handler 1996 for details). The exact implementation of the force in the present case is given in Appendix A. The configuration of the computational domain is shown in figure 6.

The equations of motion are non-dimensionalized by choosing a velocity scale, $u^* = (\mathscr{A}H/\rho)^{-1/2}$, where $\mathscr{A}$ is the amplitude of the impulsive force, and ρ is the density. The length scale is given by H (the half-height of the computational domain), and the time scale is $t^* = H/u^*$. With this scaling, the equations are solved in rotational form given by

$$\frac{\partial \boldsymbol{u}}{\partial t} = \boldsymbol{u} \times \boldsymbol{\omega} - \nabla \pi + \frac{1}{R^*}\nabla^2 \boldsymbol{u} + f\hat{\boldsymbol{e}}_z, \tag{3.1}$$

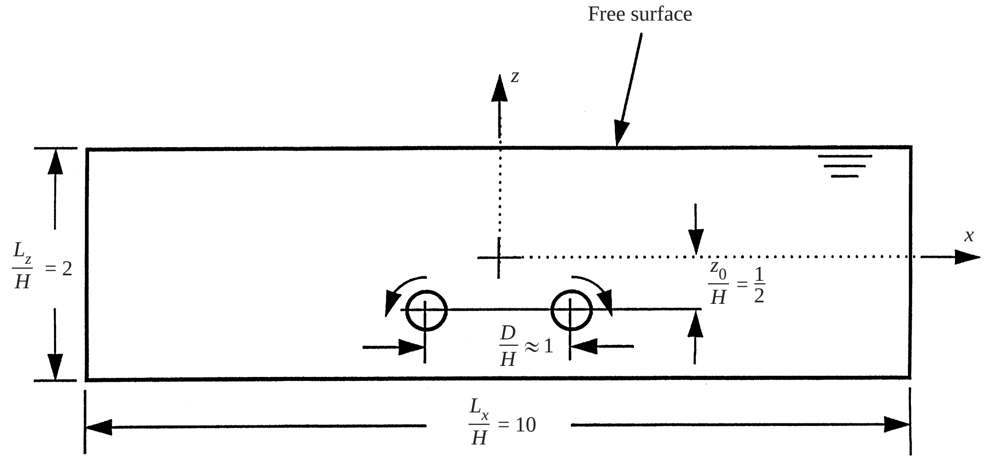

FIGURE 6. Schematic depicting the domain of the numerical simulations. Also noted are the initial positions of the vortices generated beneath the surface.

and

$$\nabla \cdot \boldsymbol{u} = 0, \tag{3.2}$$

where $\boldsymbol{u} = \boldsymbol{V}/u^*$, $\boldsymbol{\omega} = \boldsymbol{\Omega} t^*$, $\pi = p/(\rho u^{*2}) + \frac{1}{2}(\boldsymbol{u} \cdot \boldsymbol{u})$, $R^* = u^* H/\nu$, p is the pressure, ν is the kinematic viscosity, and f is a non-dimensional body force. In (3.1) and (3.2), and subsequently, the independent variables x, y, z and t are assumed to be non-dimensionalized by H and t^*.

The vortex-pair Reynolds number can be estimated *a priori* by using a linearized analysis of the vorticity produced by an impulse (see McCormack & Crane 1973). The analysis yields

$$Re = \frac{\Gamma}{\nu} \sim R^* \left(\frac{\delta_F}{H}\right)\left(\frac{u^* T}{H}\right), \tag{3.3}$$

where T is the temporal duration of the impulse and δ_F is the vertical extent of the force. In all simulations we have chosen $R^* = 10^4$, $\delta_F/H = 0.2$, and $u^* T/H = 0.75$ so that (3.3) gives $Re_{pair} \sim 1500$. This Reynolds number is approximately halfway between the low and high values determined in the experiment and thus represents a reasonable value for the numerical simulations.

The boundary conditions which are applied at $z = +1$ are those for a surfactant-contaminated surface with no surface deformation and are given by (Tsai 1996; Sarpkaya 1996)

$$w = 0, \tag{3.4}$$

$$-\frac{1}{R^*}\frac{\partial u}{\partial z} + \frac{1}{We}\frac{\partial \sigma}{\partial x} = 0, \tag{3.5}$$

where (3.4) expresses the zero deformation condition, and (3.5) determines the tangential stress balance at the interface. Here, $We = (\rho u^{*2} H)/\sigma_0$ is the Weber number based on the equilibrium surface tension, σ_0. In (3.5) and henceforth σ denotes the surface tension made non-dimensional by its equilibrium value. The constitutive model for the surfactant is given by a linearized model (Tsai 1996; Barger 1991):

$$\sigma = Ma(1 - \gamma) + 1, \tag{3.6}$$

where γ is the surfactant concentration scaled by the equilibrium concentration γ_0, and $Ma = -(\mathrm{d}\sigma/\mathrm{d}\gamma)|_0$ is the Marangoni number, where the subscript 0 denotes evaluation at the equilibrium point $\sigma = \gamma = 1$. Note that with this definition, the Marangoni number will be positive for all typical surfactant materials.

The evolution of the surfactant is assumed to be governed by the advection diffusion equation:

$$\frac{\partial \gamma}{\partial t} + \frac{\partial (u\gamma)}{\partial x} = \frac{1}{Pe}\frac{\partial^2 \gamma}{\partial x^2}, \tag{3.7}$$

where $Pe = u^*H/\alpha_s$ is the Péclet number for the surfactant, α_s is the surfactant diffusivity, and u in this relation denotes the *surface* velocity. The surfactant is assumed to be insoluble. We note that setting $Ma = 0$ results in the shear free boundary condition $\partial u/\partial z = 0$ at $z = +1$, which we employ in one set of simulations. In another set, we use the no-slip condition $u = w = 0$ at $z = +1$.

The Weber number was chosen to correspond as closely as possible to the experiment (see Appendix B) and was set to 90 in all simulations. The simulations span three orders of magnitude in Marangoni number (2.5×10^{-1} to 2.5×10^{-4}, see table 1) where $Ma = 2.5 \times 10^{-1}$ represents a highly contaminated surface (see Barger 1991) and the lower limit, a surface which is virtually clean. The Péclet number is chosen so that surfactant diffusion is relatively small during a typical hydrodynamical time scale (see Appendix B).

Along with the equations of motion, we solve the convective–diffusion equation for the temperature field given by

$$\frac{\partial \theta}{\partial t} + u\frac{\partial \theta}{\partial x} + w\frac{\partial \theta}{\partial z} = \frac{1}{R^*Pr}\nabla^2\theta + s, \tag{3.8}$$

where θ is the non-dimensional temperature ($\theta = (\Theta - \Theta_b)k/(q_oH)$), Θ is the temperature, Θ_b is the temperature at $z = -1$, k is the thermal conductivity, q_0 is the magnitude of the heat flux applied at $z = +1$, and $Pr = \nu/\alpha$ is the Prandtl number where α is the thermal diffusivity of the fluid. The Prandtl number was set to 6 in all simulations to match experimental conditions. A source term, $s = [\alpha/(q_o u^*)]S$, where S is a volumetric heat source (given in $\mathrm{W\,m^{-3}}$), has been added to achieve a desired steady-state temperature profile. The boundary conditions for the temperature field are given by

$$\frac{\partial \theta}{\partial z} = -1, \quad z = +1, \tag{3.9}$$

and

$$\theta = 0, \quad z = -1, \tag{3.10}$$

which are equivalent to a constant heat flux, q_0, directed out of the top boundary and a constant temperature, Θ_b, maintained at the bottom boundary. These boundary conditions match, as closely as possible, the experimental situation where heat is being removed from the free surface at a constant rate due to evaporative cooling.

The initial temperature in the domain is chosen by following the surface renewal analysis of Howard (1966). Combining that model with the work of Katsaros *et al.* (1977) and Liu & Businger (1975), the steady-state non-dimensional temperature profile, θ_{ss}, is given by

$$\theta_{ss} = -8\frac{\Delta}{H} i^3\mathrm{erfc}\left[\frac{(1-z)H}{2\Delta}\right], \tag{3.11}$$

where Δ is the thermal boundary layer thickness given by $\Delta = (\alpha\tau_r)^{1/2}$, and τ_r is

Run	Ma	δ	Free surface ($z=+1$)	Bottom ($z=-1$)
1	–	0.10	no-slip	no-slip
2	–	0.25	no-slip	no-slip
3	–	0.50	no-slip	no-slip
4	–	0.10	no shear	no-slip
5	–	0.25	no shear	no-slip
6	–	0.50	no shear	no-slip
7	2.5×10^{-1}	0.10	surfactant	no-slip
8	2.5×10^{-1}	0.25	surfactant	no-slip
9	2.5×10^{-1}	0.50	surfactant	no-slip
10	2.5×10^{-2}	0.10	surfactant	no-slip
11	2.5×10^{-3}	0.10	surfactant	no-slip
12	2.5×10^{-4}	0.10	surfactant	no-slip

TABLE 1. Parameters used for all of the simulations. Ma represents the Marangoni number (defined in equation (3.6)) and δ denotes the thermal boundary layer thickness (as defined in Appendix C).

the surface renewal time. The simulations were chosen to cover a range of boundary layer thicknesses, $\delta = \Delta/H = 0.1$, 0.25, and 0.5, which adequately cover the experimental conditions (see Appendix C). A plot of the steady-state temperature profiles corresponding to the three boundary layer thicknesses are shown in figure 7. It is evident that the surface temperature becomes increasingly cooler than the bulk as the boundary layer thickness increases due to the imposition of a constant (negative) heat flux at the free surface. The thermal energy source is given by the relation:

$$s = -\frac{1}{R^*Pr}\frac{\partial^2\theta_{ss}}{\partial^2 z}, \tag{3.12}$$

so that θ_{ss} will be a steady-state solution to (3.8) for the case in which the fluid is at rest. In effect, the source given by (3.12) models the buoyancy-instability process which maintains a statistically steady temperature profile.

3.2. *Numerical methods*

The equations of motion (3.1)–(3.2) and the evolution equation for the surfactant (3.7) were solved simultaneously with the heat transfer equation (3.8). This system was solved using a pseudo-spectral approach in which the velocity and temperature fields are expanded in Fourier modes in x and Chebyshev modes in z.

A fourth-order system for w is solved using a Green function approach (Orszag & Patera 1981; Kim, Moin & Moser 1987; and Handler, Hendricks & Leighton 1989). With this formulation, a boundary condition in addition to (3.4) is required for w on $z = +1$ and can be found using (3.2) and (3.5):

$$\frac{\partial^2 w}{\partial^2 z} = -\frac{R^*}{We}\frac{\partial^2\sigma}{\partial^2 x}, \quad z = +1. \tag{3.13}$$

This reduces to $\partial^2 w/\partial^2 z = 0$ at a shear-free boundary. At the bottom boundary, $z = -1$, we employ no-slip conditions $u = w = 0$ and $\partial w/\partial z = 0$.

Crank–Nicolson time-stepping is used for the diffusion operator and a second-order Adams–Bashforth scheme is used for the nonlinear terms. The Courant–Friedrichs–

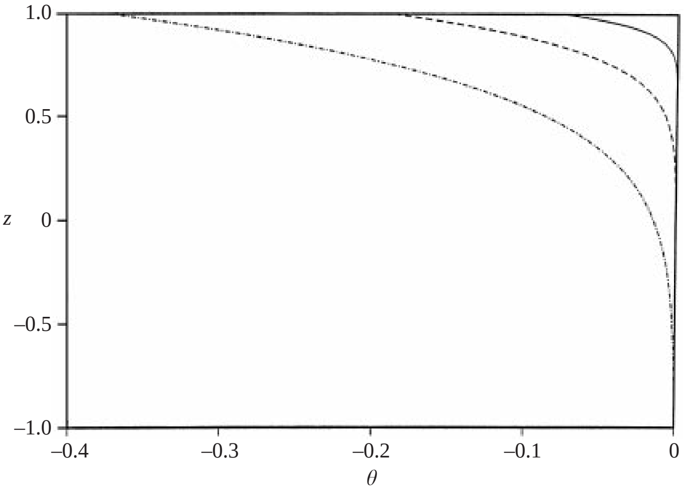

Figure 7. Steady-state temperature profile as determined from (3.11). The solid line (——) represents the thinnest thermal boundary layer, $\delta = 0.1$; the dashed line (- - -) the middle case, $\delta = 0.25$; and the dash-dot line (– · – · –) the thickest, $\delta = 0.5$.

Lewy (CFL) number, defined by

$$CFL = \Delta t \max_{(x,z)} \left[\frac{|u|}{\Delta x} + \frac{|w|}{\Delta z} \right], \tag{3.14}$$

never exceeded 0.2 in any simulation. The calculations for the velocity, temperature, and surfactant fields were fully dealiased in the Fourier direction using the 3/2 rule. The resolution was 512×65 in the x- and z-directions respectively. The initial conditions were $u(x,z) = w(x,z) = 0$ and $\theta(x,z) = \theta_{ss}$. At $t = 0$, the impulsive body force is applied and we note that its duration, $Tu^*/H = 0.75$, is small compared to the total computational time, which was 105 for all runs.

3.3. *Simulation results*

3.3.1. *Vortex trajectories*

The simulations are divided into two groups (table 1): those without surfactants (runs 1–6) and those with surfactants (runs 7–12). The parameters were selected to span a wide range of conditions, from a no-slip boundary to a shear free boundary. The surfactant simulations can be viewed as intermediate between these two regimes, even though the surfactant is advected by the surface flow, giving rise to the formation of concentration gradients, and resulting in a complex surface stress field.

Before proceeding we note that while the changing boundary conditions are the primary focus here, the effect of changes in the equilibrium thermal boundary layer thickness were also explored. It was found that as the equilibrium thermal boundary layer thickness decreased the surface temperature responded faster to the imposed straining. This is simply due to the smaller diffusional time scale, $t_d \sim \Delta^2/\alpha$, associated with a thinner thermal boundary layer.

In figure 8, the trajectories of the point of maximum vorticity of the primary vortex pair are shown for a variety of surface boundary conditions. For the case of a shear free boundary it is clear that the vortex pair does not rebound from the surface, but continues along a straight trajectory parallel with the surface. This is in agreement with the numerical simulations of Orlandi (1990) who showed that for viscous flow

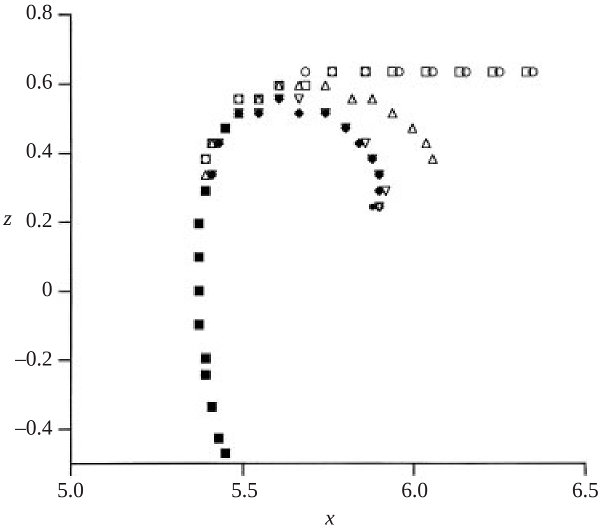

FIGURE 8. Vortex trajectories for the right-hand vortex from various free surface boundary condition runs: ○, no-shear (run 4); □, *Ma* = 2.5×10^{-4} (run 12); △, *Ma* = 2.5×10^{-3} (run 11); ▽, *Ma* = 2.5×10^{-2} (run 10); ◇, *Ma* = 2.5×10^{-1} (run 7); ●, no-slip (run 1).

along a strictly shear free boundary, no rebound takes place, although the pair does lose energy due to viscous dissipation. For the case of very weak surface elasticity, $Ma = 2.5 \times 10^{-4}$, the trajectory is virtually identical to the shear free boundary. In this case the vortex core velocity is slightly reduced relative to the shear free case. This slow down becomes evident as the vortex pair interacts with the surfactant-contaminated surface, generating viscous surface forces opposing its lateral motion.

At the other extreme, the trajectory for the no-slip boundary condition shows a strong rebound from the wall. This rebound has been observed in experiments of Walker *et al.* (1987) and in other numerical investigations (Swearingen *et al.* 1995) and is due to separation and complete ejection of boundary layer fluid from the wall. This fluid then forms a secondary vortex, which couples with the primary one, and the system moves away from the wall due to vortex mutual induction. It is evident from figure 8 that the trajectories for $Ma = 2.5 \times 10^{-1}$ and $Ma = 2.5 \times 10^{-2}$ are virtually the same as for the no-slip case. In fact, in these cases the velocities tangent to the surface were quite small (of order 5×10^{-4} and 5×10^{-3} respectively), indicating that a no-slip wall is a reasonable approximation. We note for comparison that fluid velocities in the vicinity of the primary vortex are of order 10^{-1}. At $Ma = 2.5 \times 10^{-3}$, the trajectory is intermediate between that for a no-slip and that for a shear free boundary. In this case, the vortex does exhibit a clear rebound, though weaker than for a no-slip wall.

The trajectories described above reveal the somewhat unexpected result that in spite of a reduction in surface elasticity by two orders of magnitude (2.5×10^{-1} to 2.5×10^{-3} for *Ma*), the vortex pair continues to respond as if the surface were a rigid (no-slip) wall. This was made most apparent in the case for which the surface contamination was small ($Ma = 2.5 \times 10^{-3}$), in which secondary vorticity was generated and vortex rebound was evident. In addition, there is a rather narrow range of surface elasticities (2.5×10^{-3} to 2.5×10^{-4} for *Ma*) in which the response of the vortex pair undergoes a transition from that associated with the presence of a rigid wall, to that associated

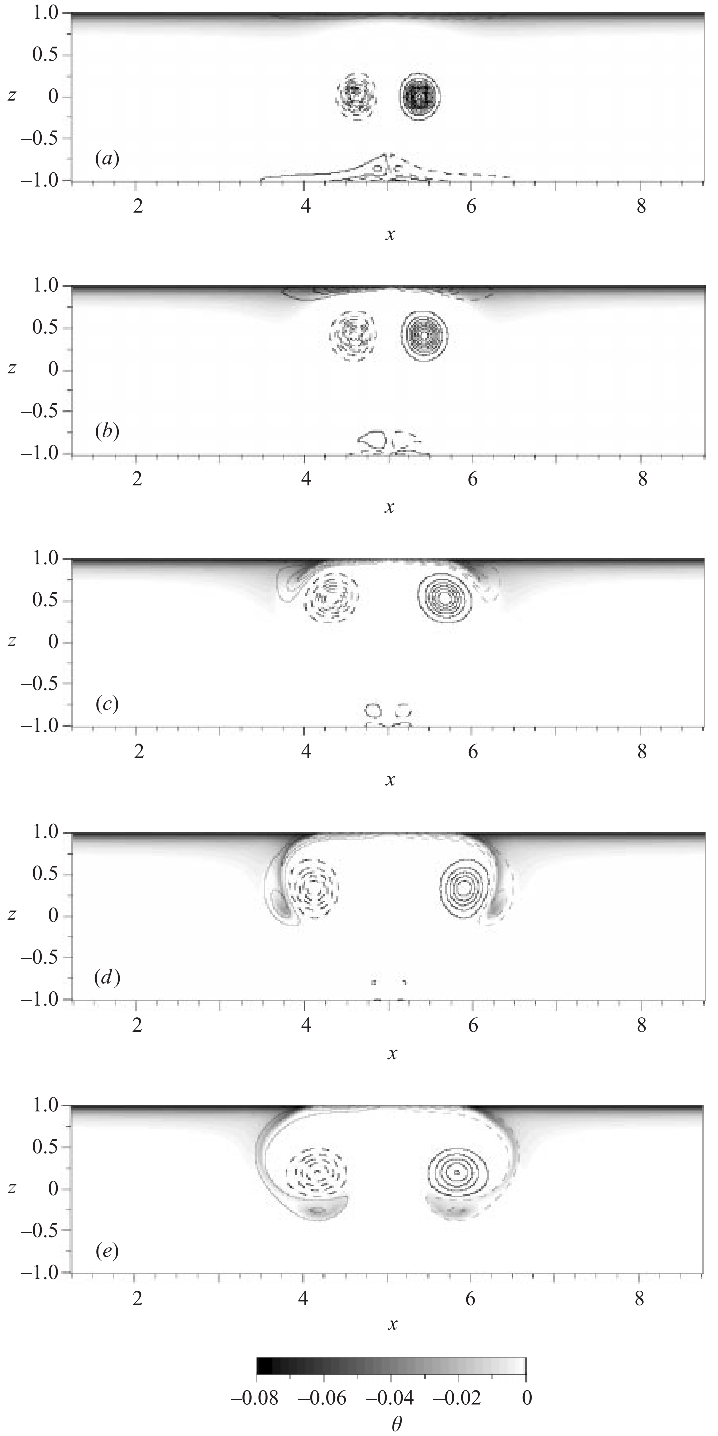

FIGURE 9. For caption see facing page.

with a stress free boundary. In summary, the response of the vortex pair to surface contamination is a continuous, but strongly nonlinear function of surface elasticity. This is principally due to the fact that even in the case of low surface elasticity, there can be an initial rapid pile up of surfactant at the outer edge of the vortex which can lead to the generation of an intense vortex sheet at the interface, separation of the sheet, and the formation of a secondary vortex. These results appear to be in good qualitative agreement with those of Tsai & Yue (1995).

3.3.2. *Dynamics of the vorticity and temperature fields*

A qualitative understanding of the dynamics can be obtained by visualizing the vorticity and the temperature fields simultaneously. In figure 9 we show the temperature field in grey scale superimposed on contours of constant vorticity for run 7 ($Ma = 2.5 \times 10^{-1}$). It is evident from figure 9(*a*) that as the vortex pair approaches the surface, a viscous boundary layer manifests itself as sheets of opposite sign vorticity on either side of the centreline. The flow at the surface contains a stagnation point at $x = 5$, implying that $\partial u/\partial x = -\partial w/\partial z > 0$. This straining field is consistent with a stretching of fluid elements in the vicinity of the stagnation point. At this time it is clear that the thermal boundary layer thickness has decreased in this region of surface divergence. The vorticity on the bottom wall is generated during the vortex generation process and has no effect on the subsequent dynamics. In figure 9(*b*) the vortex sheet has become more intense and the thermal boundary layer has been reduced dramatically in thickness near the point of symmetry, while it has begun to thicken at the outer edge of the vortex. A detailed analysis of the surface velocity field shows that this thickening is due to a negative straining, $\partial u/\partial x < 0$, or surface *convergence*. During the period seen in (*c*) to (*e*) the boundary layer fluid is advected from the surface, and forms a secondary vortex pair as the primary vortex shows a clear rebound from the boundary. These results are very similar to those described in figures 4 and 5, where the vorticity fields from the experimental runs are shown.

The unsteady separation process causing the formation of a secondary vortex is due to the development of an adverse pressure gradient along the boundary (Walker *et al.* 1987). This pressure gradient results from the expansion of the flow around the outer edge of the primary vortex and is associated with a surface convergence ($\partial u/\partial x < 0$), as mentioned earlier. Thus, it is not surprising that the thickening of the thermal boundary layer should be associated with the formation of secondary vorticity. The formation of a secondary vortex also coincides with the formation of cold cores of fluid which have been pulled down from the surface into the bulk fluid. The centres of these cores are evident at $z \simeq 0.2$ and $z \simeq -0.2$ in figure 9(*d*) and 9(*e*) respectively. It is apparent that these concentrated regions of cold fluid closely coincide with the maxima in the secondary vorticity which has separated from the surface. This follows, since for this strictly two-dimensional flow, the temperature and the vorticity satisfy the same convective–diffusion equation, if the temperature source (see (3.12)), which is

FIGURE 9. The temporal evolution of the vorticity and temperature fields in a plane perpendicular to the free surface for run 7 of the simulations. See table 1 for the corresponding flow parameters. The solid and dashed lines represent positive and negative vorticity, respectively. The outermost contours represent non-dimensionalized vorticity magnitude of ± 0.1, and the vorticity increments by 0.2 for each contour. Non-dimensional temperature (θ, defined in equation (3.8)) is represented by shades of grey. The non-dimensional times for the images in the sequence (with 0 being the start of the simulation) are as follows: (*a*) $t = 26.25$; (*b*) $t = 45$; (*c*) $t = 63.75$; (*d*) $t = 82.5$; and (*e*) $t = 101.25$.

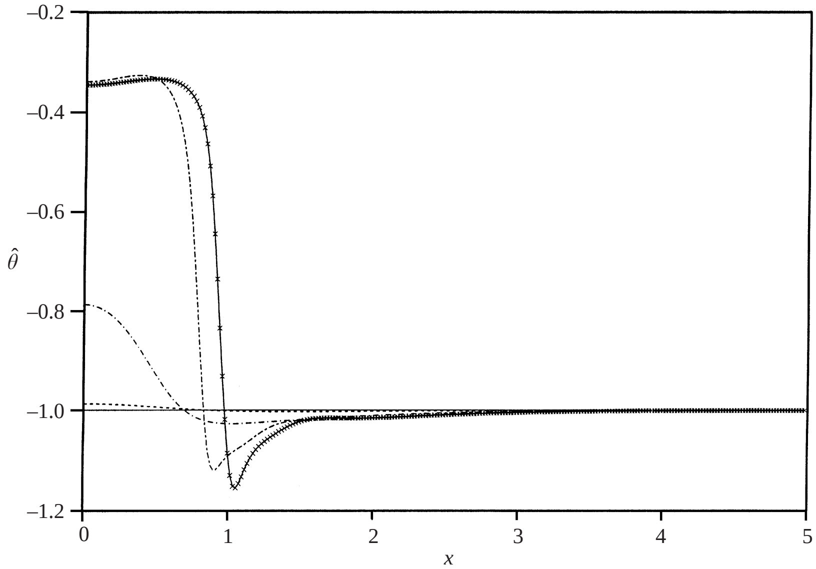

FIGURE 10. Temporal evolution of surface temperature for run 7 ($Ma = 2.5\times10^{-1}$) of the simulations. The horizontal axis denotes distance from the centreline of the domain, and the vertical axis represents non-dimensional temperature at the water surface. The non-dimensional temperature is defined by $\hat{\theta} = (\Theta - \Theta_b)/|\Theta_s - \Theta_b|$, where Θ_b is the temperature of the bulk and Θ_s is the initial surface temperature. Thus, at $t = 0$, $\hat{\theta} = -1$. The plotting symbols represent different times in the simulation: - - -, $t = 15$; –·–·–, $t = 45$; –––––, $t = 75$; –×–, $t = 101.25$.

small far from the surface, is neglected. In addition, since diffusion can reasonably be neglected for the short time intervals being considered, both the temperature field and the secondary vortex core must follow the fluid particle motion around the primary vortex.

The time history of the surface temperature profiles are shown in figure 10, where the non-dimentional temperature, $\hat{\theta}$ is defined as $\hat{\theta} = (\theta - \theta_b)/|\theta_s - \theta_b|$. Here θ_b has been fixed ($\theta_b = 0$) and θ_s is defined as the initial surface temperature, so that at $t = 0$, $\hat{\theta} = -1$. Several significant characteristics are seen therein. First, the temperature at the centreline rises monotonically in time until it attains a peak value of $\hat{\theta} = -0.32$. Thus the surface centreline temperature reaches approximately 70% of the bulk temperature and will naturally cool back to the initial ($\hat{\theta} = -1$) temperature. A second important feature is the drop in surface temperature below that of the initial surface temperature in the vicinity of $x \simeq 1$. The minimum in $\hat{\theta}$ tends to move away from the centreline as time increases and attains a value of about $\hat{\theta} = -1.16$, significantly lower than the equilibrium surface temperature. The size and magnitude of the thermal scar generated during the simulations are in good agreement with the experiment where both the strong rise in centreline temperature and the cooling in a thin region at the outer edge of the vortex pair were observed. These results compare qualitatively quite well with the surface temperature profiles obtained during the experiments shown in figure 5.

3.3.3. *Relation between surface strain and temperature*

It has been posited that the instantaneous thermal boundary layer thickness, and consequently the surface temperature, is primarily dependent on the sub-surface strain

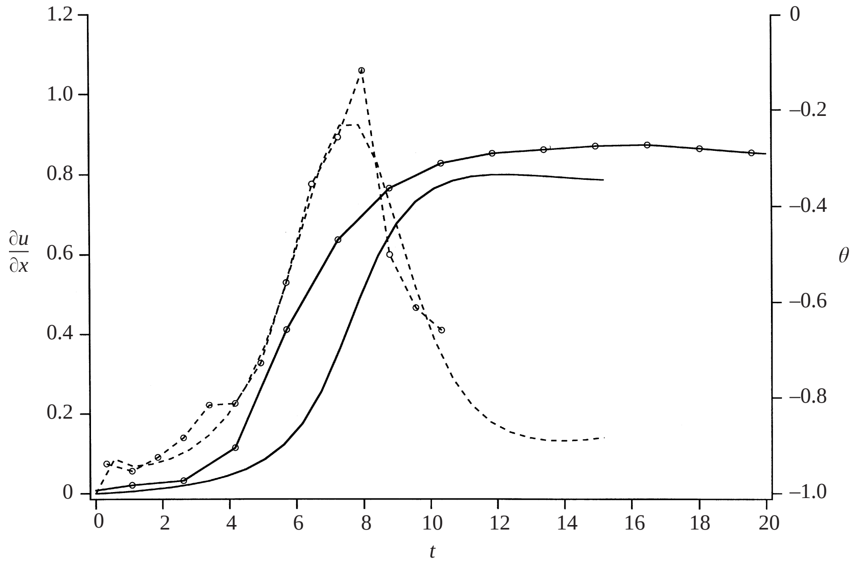

FIGURE 11. Centreline surface temperature (solid lines) and rate of strain (dashed lines) for both the simulations (no symbols) and experiments (open circles). The left-hand axis displays the rate of strain, non-dimensionalized by the initial circulation and vortex separation, and the right-hand axis displays the non-dimensional temperature, defined as $\hat{\theta} = (\Theta - \Theta_b)/|\Theta_s - \Theta_b|$, where Θ_b is the temperature of the bulk and Θ_s is the initial surface temperature. Due to differences between the startup of the experiments and simulations $t = 0$ is poorly defined. To compensate, the experimental data have been shifted. Time have been non-dimensionalized by the initial vortex separation distance and circulation for both the experiments and simulations.

field. To illustrate this point, direct comparisons of the rate of strain at the surface and surface temperature, for both the experiments and simulations, are presented.

Figure 11 contains the centreline surface temperature and rate of strain data for both the high *Re* experimental run and the moderately contaminated simulation (case 7). All the data are plotted against the same time axis; however, due to differences in the vortex generation process for the experiments and simulations, an arbitrary 'd.c.' shift of the experimental data along the time axis was required. The experimental data were shifted until the strain rate signatures matched those from the simulations. It should be emphasized that the shift was purely an offset – the slopes or shapes of the signatures were not altered by the shift.

First examination reveals the excellent agreement between the experimental and computational data sets. The shape of the strain rate signatures is almost identical in both cases. The strain rate exhibits roughly symmetric behaviour, rising to a peak as the vortex pair approaches the surface, and decaying rapidly after the interaction.

The centreline surface temperatures for the experiments and simulations also agree quite well, both rising rapidly behind the sudden increase in strain. In both cases the peak in strain rate at the surface precedes the peak in surface temperature, but the experimental result does show a slightly faster surface temperature response to the increase in strain. One possible source for the slight differences which appear between the simulation and experiment is a slight lack of symmetry in the vortices in the experiment. The interaction of the slightly tilted vortices with the secondary vorticity generated at the surface, along with any smaller scale instabilities, may generate more complex, longer lasting structures, which maintain the strain on the thermal boundary layer. This is supported by the centreline surface temperature signature, where the experimental surface temperature does not decay as rapidly as in the simulation.

While early in the interaction there is a rapid temperature rise, the cooling of the surface in both cases takes place at a much slower rate. This indicates that there are two important time scales in the problem. During the initial phase of the interaction, while the vortices are approaching or have just reached the surface, it is convective processes which drive the flow. The near surface fluid is strained by the vortex pair and bulk fluid is driven to closer proximity to the free surface. In the later stages of the interaction, as the strain decays, the amount of heat transport due to convective motions decreases, until the heat transport due to diffusion can roughly balance it. It is at this point that the surface temperature peaks. As the vortex pair dissipates, and the strain field further decays, the surface temperature equilibrates. This process occurs on the much slower diffusional time scale.

To summarize, there are three phases to the vortex–free surface interaction. Initially the process is governed by convective straining effects. This is followed by an equilibrium period, and finally a diffusion-dominated recovery to steady state. This is supported by both the experiments and the simulations, and by the very close agreement between the two.

4. Summary and conclusions

The interaction between a thermal boundary layer at an air–water interface and a rising vortex pair was investigated. The objective was to determine the relationship between the apparent thermal structure of the interface and the hydrodynamics below. This was achieved through a combination of experimental and computational methods.

In both the experimental and numerical studies a pair of line vortices was generated beneath the water surface and allowed to propagate upward under their own mutual induction. In both cases as the primary vortices approached the interface they disrupted the cool skin present at the surface, producing a region of warmer surface temperature. Contamination of the surface in the experiments allowed secondary vorticity to be formed at the interface, causing the primary vortices to separate and rebound from the interface. For comparison, simulations were run with a simple surfactant model, and with a shear free and a no-slip boundary. The numerical results provided detailed data on the source of the warm thermal scar produced by the vortex interaction, along with the rebound and ejection of cool boundary layer fluid from the surface into the bulk.

The manner in which the perturbations of the sub-surface flow manifest themselves in the thermal structure of the interface is explained with a simple model based on surface straining rate. Essentially, when a divergent (positive rate of surface strain) condition exists near the surface the thermal boundary layer is thinned, resulting in a higher surface temperature. In a convergent flow, the opposite occurs. In the case of the rising vortex pair, there is a strong divergence in the region between the primary vortices which causes a rapid thinning, and in some cases, almost a total rupture of the thermal boundary layer in that region. This results in a relatively warm elongated scar in the free surface temperature field. This scar is commonly outlined by a thin filament of cooler fluid which corresponds with a region of convergence.

In conclusion, the significant findings resulting from this work can be listed as follows:

(i) as expected, very rich thermal structure is present in a seemingly quiescent free surface, even under low heat flux conditions;

(ii) this ambient structure is dynamically significant in sufficiently low Reynolds number flows;

(iii) the small-scale instabilities which appear at higher Reynolds number bear a striking resemblance to surface deformations reported by Sarpkaya & Suthon (1991);

(iv) the simulations suggest that even for very small values of Marangoni number ($Ma \sim 10^{-3}$) the free surface behaves much like a solid boundary;

(v) and finally, the comparisons between the simulations and experiments allowed three primary conclusions:

> first, the high degree of agreement between the simulations and experiments confirms that the simulations captured the important physical processes occurring during the interaction;
>
> secondly, three time scales can be identified during the interaction: an initial convective scale, a final diffusional time scale, and an intermediate scale which is associated with a balance between the surface straining rate and the diffusion rate;
>
> lastly, the simulations also confirm the validity of the surface strain model for the case of a vortex pair interaction with a free surface.

The authors gratefully acknowledge the support of the Office of Naval Research, through the Naval Research Laboratory and the Naval Academy Research Council, the US Naval Academy–Naval Research Laboratory cooperative agreement, and the computational support of the DOD High Performance Computing Program.

Appendix A. Specification of the impulsive body force

The impulsive force in the simulation is given by

$$F(x,z,t) = \mathscr{A}\mathscr{X}(x)\mathscr{Z}(z)\mathscr{T}(t) \tag{A 1}$$

where

$$\mathscr{X}(x) = \tfrac{1}{2}[1 + \tanh \alpha(a_x - a(x))], \tag{A 2}$$

$$\mathscr{Z}(z) = \tfrac{1}{2}[1 + \tanh \beta(a_z - b(z))], \tag{A 3}$$

$$\mathscr{T}(t) = \tfrac{1}{2}[1 + \tanh \gamma(a_t - c(t))], \tag{A 4}$$

and

$$a(x) = \sqrt{(x-x_0)^2}, \quad b(z) = \sqrt{(z-z_0)^2}, \quad c(t) = \sqrt{(t-t_0)^2}, \tag{A 5}$$

where $\mathscr{A}$ is the amplitude of the force, $2a_x$, $2a_z$, and $2a_t$ denote the approximate extent of the force in the x- and z-directions and in time, x_0, z_0, and t_0 denote the spatial and temporal origin of the force, and α, β, and γ specify the degree of smoothing applied to the edges of the force field.

Appendix B. Determination of the surfactant diffusivity and Weber number

In the simulation, $D/H \simeq 1$ where D is defined to be the initial separation between the centres of the vortices, and in the experiment, $D \simeq 1.5\,\mathrm{cm}$, so that $H \simeq 1.5\,\mathrm{cm}$. The velocity scale can be determined from, $u^* = R^*\nu/H = 66.6\,\mathrm{cm\,s^{-1}}$, where $R^* = 10^4$, and

$\nu = 0.01\,\mathrm{cm^2\,s^{-1}}$. Thus the Weber number can determined as $We = \rho u^{*2}H/\sigma_0 \simeq 90$, where $\rho = 1\,\mathrm{g\,cm^{-3}}$, and $\sigma_0 = 72.75\,\mathrm{dyn\,cm^{-1}}$.

The Péclet number is chosen so that the surfactant diffuses a negligible distance during a typical hydrodynamical time scale. This requires $\delta/D \ll 1$, where δ is the distance the surfactant will diffuse in a typical eddy turnover time, T_{eddy}. Using this criterion the following estimates can be made:

$$\frac{\delta}{D} \simeq \sqrt{\frac{\alpha_s T_{eddy}}{D^2}}, \tag{B 1}$$

$$T_{eddy} \simeq \frac{2\pi r}{u}, \tag{B 2}$$

where r is the radius of the vortex core, and u is the tangential fluid velocity at the outer edge of the core. The Péclet number can be written as

$$Pe = \frac{u^* H}{\alpha_s} = \left(\frac{D}{\delta}\right)^2 \left(\frac{2\pi(r/D)}{(D/H)}\right) \frac{u^*}{u}. \tag{B 3}$$

From the simulations we find $r/D \simeq 0.2$ and $u/u^* \simeq 0.1$ so that the Péclet number can now be estimated from (B 3) as $Pe \simeq 12.6(D/\delta)^2$. For the simulations we have chosen $Pe = 1000$ which correspond to $\delta/D \leqslant 0.1$ as required.

Appendix C. Determination of the thermal boundary layer thickness

The expression for the non-dimensional thermal boundary layer thickness, δ, in terms of the heat flux and the surface–bulk temperature difference is given by

$$\delta = \frac{\Delta}{H} = \frac{3\sqrt{\pi}}{4}\frac{L}{H}, \tag{C 1}$$

where

$$L = \frac{k(\Theta_s - \Theta_b)}{q_0}, \tag{C 2}$$

and Θ_s and Θ_b are the surface and bulk temperatures for the steady-state profile given by (3.11). In the experiment, $\Theta_s - \Theta_b \simeq 0.5\,\mathrm{K}$, $q_0 \simeq 60\,\mathrm{W\,m^{-2}}$, $k = 0.6\,\mathrm{W\,m^{-1}\,K^{-1}}$, so that $L \simeq 5 \times 10^{-3}\,\mathrm{m}$. In addition, it can be shown that $L/H \simeq 1/3$ matches experimental conditions so that $\delta \simeq (1/3)(3\sqrt{\pi}/4) = 0.44$ from (C 1). Accordingly, the simulations were chosen to cover a range of boundary layer thicknesses, $\delta = 0.1, 0.25$, and 0.5, which should adequately cover the experimental conditions.

REFERENCES

Asaeda, T. & Watanabe, K. 1989 The mechanism of heat transport in thermal convection at high Rayleigh numbers. *Phys. Fluids* A **1**, 861–867.

Barger, W. R. 1991 A review of experimental observations and remaining questions concerning formation, persistence and disappearance of sea slicks. *Naval Research Laboratory Rep.* 9313.

Bernal, L. P., Hirsa, A., Kwon, J. T. & Willmarth, W. W. 1989 On the interaction of vortex rings and pairs with a free surface for varying amounts of surface active agent. *Phys. Fluids* A **1**, 2001–2004.

Chen, Z., Swearingen, J. D. & Handler, R. A. 1996 Vortex ring interaction with an inclined wall. *Proc. ASME Fluids Engng Conf.*, Vol. 238, pp. 57–64.

Donlon, C. J. & Robinson, I. S. 1997 The role of breaking wavelets in air-gas transfer. *J. Geophys. Res.* **95**, 749.

Goldstein, R. J. & Volino, R. J. 1995 Onset and development of natural convection above a suddenly heated horizontal surface. *J. Heat Transfer* **117**, 808–821.

Handler, R. A., Hendricks, E. W. & Leighton, R. I. 1989 Low Reynolds number calculation of turbulent channel flow: a general discussion. *Naval Research Laboratory Mem. Rep.* 6410.

Hirsa, A., Korenowski, G. M., Logory, L. M. & Judd, C. D. 1997 Velocity field and surfactant concentration measurement techniques for free-surface flows. *Exps. Fluids* **22**, 239–248.

Hirsa, A. & Willmarth, W. W. 1994 Measurements of vortex pair interaction with a clean or contaminated free surface. *J. Fluid Mech.* **259**, 25–45.

Howard, L. N. 1966 Convection at high Rayleigh number. *Proc. Eleventh Intl Congress of Applied Mechanics, Munich, Germany, 1964* (ed. H. Gortler), pp. 1109–1115. Springer.

Katsaros, K. B., Liu, W. T., Businger, J. A. & Tillman, J. 1977 Heat transport and thermal structure in the interfacial boundary layer measured in an open tank of water in turbulent free convection. *J. Fluid Mech.* **83**, 311–335.

Kim, J., Moin, P. & Moser, R. 1987 Turbulence statistics in fully developed channel flow at low Reynolds number. *J. Fluid Mech.* **177**, 133–166.

Leighton, R. I. & Smith, G. B. 2001 Parametric modeling of the thermal boundary layer. *J. Geophys. Res.* (in press).

Leighton, R. I., Smith, G. B. & Tang, S. 1998 A comparison of simulated and experimental IR measurements at low to moderate wind speed. In *1998 IGARSS Sympo. Proc.* Vol. 1, pp. 481–483.

Liu, T. W. & Businger, J. A. 1975 Temperature profile in the molecular sublayer near the interface of a fluid in turbulent motion. *Geophys. Res. Lett.* **2**, 403–404.

Lucassen, J. 1968 Longitudinal capillary waves: Part I. Theory. *Trans. Faraday Soc.* **64**, 2221–2229.

McCormack, P. D. & Crane, L. 1973 *Physical Fluid Dynamics.* Academic.

Orlandi, P. 1990 Vortex dipole rebound from a wall. *Phys. Fluids* A **2**, 1429–1436.

Orszag, S. A. & Patera, A. T. 1981 Subcritical transition to turbulence in planar shear flows In *Transition and Turbulence* (ed. R. E. Meyer), pp 127–146. Academic.

Paulson, C. A. & Simpson, J. J. 1981 The temperature difference across the cool skin of the ocean. *J. Geophys. Res.* **86**, 11044–11054.

Rood, E. P. 1994 Interpreting vortex interactions with a free surface. *Trans. ASME: J. Fluids Engng* **116**, 91–94.

Sarpkaya, T. 1996 Vorticity, free surfaces, and surfactants. *Ann. Rev. Fluid. Mech.* **28**, 83–128.

Sarpkaya, T. & Suthon, P. 1991 Interaction of a vortex couple with a free surface. *Exps. Fluids* **11**, 205–217.

Saunders, P. M. 1969 The temperature at the ocean-air interface. *J. Atmos. Sci.* **24**, 269–273.

Saylor, J. R., Smith, G. B. & Flack, K. A. 2000 The effect of a surfactant monolayer on the temperature field of a water surface undergoing evaporation. *Intl J. Heat Mass Transfer* **43**, 3073–3086.

Smith, G. B. 1996 Turbulent transport in moderate to high Reynolds number vortex rings. PhD thesis, Rutgers, the State University of New Jersey.

Spangenberg, W. G. & Rowland, W. R. 1961 Convective circulation in water induced by evaporative cooling. *Phys. Fluids* **4**, 743–750.

Swearingen, J. D., Crouch, J. D. & Handler R. A. 1995 Dynamics and stability of a vortex ring impacting a solid boundary. *J. Fluid Mech.* **297**, 1–28.

Tsai, W. 1996 Impact of a surfactant on a turbulent shear layer under the air-sea interface. *J. Geophys. Res.* **101**, 28557–28568.

Tsai, W. & Yue, D. K. P. 1995 Effects of soluble and insoluble surfactant on laminar interactions of vortical flows with a free surface. *J. Fluid Mech.* **289**, 315–349.

Volino, R. J. & Smith, G. B. 1999 Use of simultaneous IR temperature measurements and DPIV to investigate thermal plumes in a thick layer cooled from above. *Exps. Fluids* **27**, 70–78.

Walker, J. D. A., Smith, C. R., Cerra, A. W. & Doligalski, T. L. 1987 The impact of a vortex ring on a wall. *J. Fluid Mech.* **181**, 99–140.

Weigand, A. & Gharib, M. 1995 Turbulent vortex ring/free surface interaction. *Trans. ASME: J. Fluids Engng* **117**, 374–381.

Wick, G. A., Emery, W. J., Kantha, L. H. & Schlussel, 1996 The behavior of the bulk-skin sea surface temperature difference under varying wind speed and heat flux. *J. Phys. Oceanogr.* **26**, 1969–1988.

Willart, C. E. & Gharib, M. 1991 Digital particle image velocimetry *Exps. Fluids* **10**, 181–193.

Willmarth, W. W., Tryggvason, G., Hirsa, A. & Yu, D. 1989 Vortex pair generation and interaction with a free surface. *Phys. Fluids* A **1**, 170–172.

Woodcock, A. H. 1941 Surface cooling and streaming in shallow fresh and salt waters. *J. Mar. Res.* **4**, 153–161.

Yoshimori, K., Itoh, K. & Ichioka, Y. 1994 Statistically corrected ocean thermography. *Appl. Optics* **33**, 7078–7087.